High-Temperature Materials

SCIEPublish

Article

Influence of Mo on Microstructure and High-Temperature Mechanical Properties of Fire-Resistant Steels

Lijuan Zhu [1], Chun Feng [1,2,*], Xiaolu Gui [3], Qi Ji [1] and Guhui Gao [3,*]

[1] State Key Laboratory of Oil and Gas Equipment, Tubular Goods Research Institute of CNPC, Xi'an 710077, China; zhulijuan1986@cnpc.com.cn (L.Z.); jiqi@cnpc.com.cn (Q.J.)

[2] CNPC Bohai Equipment Manufacturing Co., Ltd., Tianjin 300457, China

[3] School of Mechanical, Electronic, and Control Engineering, Beijing Jiaotong University, Beijing 100044, China; xlgui@bjtu.edu.cn (X.G.)

* Corresponding author. E-mail: fengchun003@cnpc.com.cn (C.F.); gaogh@bjtu.edu.cn (G.G.)

Received: 15 June 2026; Revised: 6 July 2026; Accepted: 7 September 2026; Available online: 24 September 2026

ABSTRACT: The long-term fire safety of steel structures necessitates fire-resistant (FR) steels with superior strength retention after prolonged exposure to elevated temperatures. This study investigates two FR steels with Mo contents of 0.25 wt.% and 0.50 wt.% (correspondingly adjusted Cr contents to maintain a nearly constant total Mo + Cr alloy level) after thermal exposure at 600 °C for up to 6 h. Both steels exhibit a polygonal ferrite (PF) and granular bainite (GB) microstructure, but with different phase fractions. Increasing Mo to 0.5 wt.% promotes bainite formation, resulting in a predominantly granular bainitic microstructure (88% GB and 12% PF). A multi-scale characterization reveals that the higher-Mo/lower-Cr design not only increases the fraction of GB but also dramatically enhances its thermal stability. Importantly, Mo suppresses the premature precipitation of coarse (Nb, Ti)(C, N) in the parent austenite, thereby retaining solutes for the subsequent precipitation of a high number density of fine carbides within the bainitic ferrite laths during thermal exposure. The combination of a high-density dislocation substructure within the stable GB and the strong precipitation strengthening from these dispersed nano-carbides is primarily responsible for the superior strength retention in the higher-Mo/lower-Cr FR3 steel. This steel maintains a high yield strength of 440 MPa after 6 h at 600 °C, which is 158 MPa higher than its 0.25 wt.% Mo counterpart and satisfies the international fire-resistance criterion (YS600 °C/YSRT > 2/3). This work provides a mechanistic basis for optimizing Mo–Cr alloy design to achieve exceptional long-term high-temperature performance in FR steels.

Keywords: Fire-resistance steel; High temperature mechanical property; Granular bainite; Microstructure; Dislocation

1. Introduction

With the deepening of oilfield development, the difficulty and complexity of operations have increased, and the unknown risk factors in development operations have become more numerous, increasing the probability of blowouts and wellhead fires. Therefore, the development of a new generation of oilfield

firefighting and rescue machinery has attracted widespread attention in the industry. However, conventional steel materials suffer from a significant degradation in mechanical strength at elevated temperatures [1,2]. The mechanical properties of steel are temperature-dependent, and its elastic modulus decreases progressively with increasing temperature. When the temperature reaches 400 °C, the yield strength of commonly used structural steel drops to half of its room-temperature value. At 600 °C, the load-bearing capacity becomes almost negligible [1,2]. To mitigate this issue, a thicker fire-resistant coating is generally applied as a protective measure [3,4].

Since the 1990s, the development of fire-resistant steel (FRS) has been pursued to provide a more economical and straightforward solution for enhancing the fire safety of buildings or machinery. These advanced steels can ensure structural fire resistance without additional costs or delays in construction. Fire-resistant steels are designed to retain a high YS at 600 °C compared to room temperature (RT), and this performance is commonly quantified using the YS ratio (600 °C/RT) [5,6]. In 1987, Japan's Architectural Committee established a critical performance criterion requiring that the high-temperature yield strength should not fall below two-thirds of its room-temperature value-a benchmark later adopted internationally [2].

Modern fire-resistant steels rely on optimized alloying and heat treatment strategies. Molybdenum (Mo) is widely recognized as the most effective alloying element for enhancing high-temperature strength [7,8], owing to its contributions to solid-solution strengthening, precipitation hardening, and the promotion of bainite formation [9]. Wan et al. [10] quantitatively evaluated the strengthening effect of bainite, reporting a 1.655 MPa increase in 600 °C yield strength per 1 vol% increase in bainite content. To improve cost efficiency, recent studies have explored partial substitution of Mo with strong carbide-forming elements such as Nb, V, and Ti, which form thermally stable precipitates that mitigate high-temperature softening. For instance, Li et al. [11] demonstrated that Nb microalloying could effectively replace Mo while maintaining performance. Walp et al. [12] designed four experimental steels, including plain carbon, Nb-modified, Mo + Nb modified, and V + Nb modified, demonstrating that Nb addition significantly improved high-temperature yield strength, with the Mo + Nb combination exhibiting optimal fire resistance. Wang et al. [13] further confirmed that multi-microalloyed steels exhibit superior mechanical properties at both room and elevated temperatures compared to single-element variants. Notably, the strengthening contributions from solid solution, precipitation, and bainite transformation are interdependent, necessitating careful optimization to maximize alloying efficiency.

Recent advancements in air-cooled bainitic steels have provided a new pathway for cost-effective fire-resistant steel production [14,15]. Unlike conventional quenching and tempering, air-cooling after hot rolling enables bainite formation while reducing energy consumption and CO_2 emissions. In this context, Mo plays a crucial role in enhancing hardenability and promoting bainitic transformation during air cooling [16,17]. However, in Nb/V/Ti-microalloyed steels, the slow cooling rates may also influence carbide precipitation kinetics, which could be further modulated by Mo additions. Moreover, the long-term stability of these microstructures under prolonged thermal exposure remains insufficiently explored.

Recent demands for fire-resistant steels have expanded to critical components in oilfield firefighting and rescue engineering machinery. These components require prolonged operation durations under complex loading conditions, necessitating enhanced fire-resistant properties—such as fire resistance durations exceeding 6 h and tolerance to temperatures surpassing 600 °C (e.g., from wellhead fires). Current design standards, however, primarily address thermal exposure at 600 °C for 3 h. Prolonged high-temperature exposure accelerates carbide coarsening and reduces dislocation density, both of which degrade high-temperature strength retention.

To address these gaps, this study comparatively investigates two Nb-bearing low-alloy steels with 0.25 and 0.5 wt.% Mo, focusing on microstructural evolution and precipitation behavior after 3 h and 6 h of thermal exposure at 600 °C, with the aim of optimizing the alloy composition and processing route to develop fire-resistant steels that exhibit superior long-term high-temperature resistance.

2. Materials and Methods

2.1. Materials

The chemical compositions of the investigated fire-resistant steel are presented in Table 1. The experimental steels were designed with different Mo and Cr combinations (0.25 wt.% Mo/1.2 wt.% Cr and 0.50 wt.% Mo/0.8 wt.% Cr). The two steels differ in both Mo and Cr contents, with the lower Cr in FR3 compensating for the reduced Mo to maintain a similar total alloying content. Additional alloying elements Nb, Ti, and V were incorporated to enhance high-temperature strength retention. The steels were produced in a 50 kg vacuum induction melting furnace. Following melting, the casting ingots were reheated at 1200 °C and forged to square billets of 60 mm × 60 mm in size. The square billets were re-homogenized at 1200 °C for 2 h and hot rolled to 12 mm thick plates with a finishing rolling temperature of ~850 °C, then air-cooled to room temperature with a cooling rate of ~1 °C/s, as shown in Figure 1.

Table 1. Chemical composition of test steels (wt.%).

Steels	C	Si	Mn	Cr	Mo	Nb	Ti	V	N	S	P	Al	Fe
FR1	0.12	0.79	1.82	1.19	0.25	0.06	0.02	0.01	0.005	0.004	0.003	0.002	Bal.
FR3	0.12	0.80	1.81	0.81	0.50	0.06	0.02	0.01	0.005	0.004	0.004	0.002	Bal.

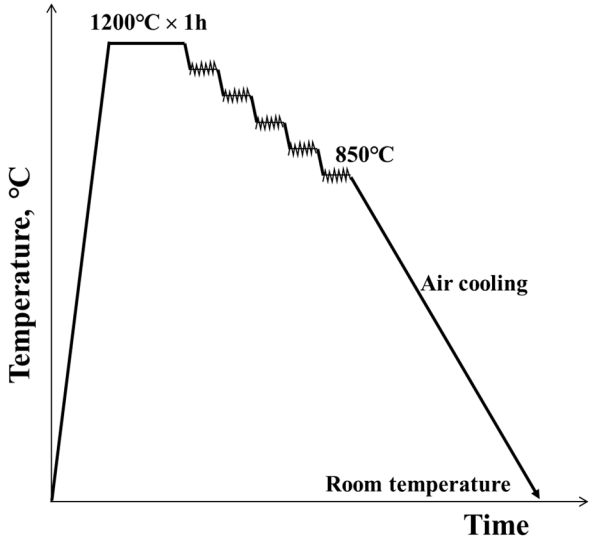

Figure 1. Schematic diagrams of hot rolling and air-cooling processes of experimental steels.

2.2. Microstructure Examination

Microstructures were characterized using a scanning electron microscope (SEM, ZEISS EVO18, Carl Zeiss Microscopy GmbH, Oberkochen, Germany) operated at 20 kV and a field emission transmission electron microscope (TEM; JEOL JEM-2020F, JEOL Ltd., Tokyo, Japan) operated at 200 kV. SEM samples were prepared by mechanical polishing and etching in a 2% Nital solution. TEM samples were prepared with 3 mm diameter thin foil, mechanically polished to approximately 50 μm thickness, and then electrochemically polished using a twin-jet electropolished at −30 °C in a 6% perchloric acid solution using an RL-I twin-jet electropolisher (Ruiling Innovation Technology Co., Ltd., Beijing, China). Precipitates were extracted using the carbon replica technique. Samples were polished and etched in 2% Nital solution, then sprayed with carbon. The carbon film with the secondary phase particles was collected using Cu mesh. The morphology, distribution, and composition of precipitate were analyzed by TEM and energy dispersive spectroscopy (EDS). The fraction and size of each phase (such as ferrite, bainite, and carbide) were quantified using Image Pro Plus 6.0 software. X-ray diffraction (XRD, Rigaku Smartlab, Cu

Kα radiation) was performed to detect the presence of RA. The diffraction patterns were obtained in the 2θ degree range of 40–120° with a step size of 0.01° and a counting time of 2 s per step. Electron backscattered diffraction (EBSD) was conducted using ZEISS EVO18 SEM operated at 20 kV with a scanning step size of 0.1 μm. Thermodynamic simulations were performed using hermo-Calc software (version 2018b, Thermo-Calc Software AB, Stockholm, Sweden) with the TCFE8 database. 3D atom probe needle tips were prepared by electrolytic polishing. 3D atom probe (3DAP) microscopy (LEAP 4000× HR, CAMECA Instruments Inc., Madison, WI, USA) was performed using laser mode. One representative tip was analyzed for each condition. The atom probe analysis was performed at a temperature of 50 K in an ultra-high vacuum ($<1 \times 10^{-8}$ Pa) at a pulse fraction of 0.15 and a pulse repetition rate of 300 Hz. Imago visualization and analysis software version 3.6 was used for 3D reconstruction and composition analyses. Due to the limited analyzed volume, quantitative comparisons focus on relative trends between the two steels rather than absolute precipitate populations.

Tensile specimens with a 25 mm gauge length and 5 mm diameter were prepared from the as-rolled plate along the transverse direction. Tensile properties were measured at both room temperature (RT, 25 °C) and at 600 °C on the SUNS 5035 tensile testing machine according to GB/T 228.1-2021 [18] for room-temperature tensile testing and GB/T 228.2-2015 [19] for elevated-temperature tensile testing. The elevated temperature tensile tests were performed directly at 600 °C. Specimens were first heated to 600 °C in a furnace integrated with the tensile testing machine and held isothermally for 3 h or 6 h. Subsequently, without cooling down, a high-temperature extensometer was mounted on the tensile samples. After holding for ~3 min to stabilize temperature and extensometer readings, tensile loading was applied at 600 °C with a strain rate of 10^{-3} s^{-1}. For both room temperature and elevated temperature tensile testing, at least four specimens were used for both steels, and the average values were recorded. All microstructural samples were extracted from the grip (unloaded) sections of tensile specimens after thermal exposure, ensuring that the observed evolution reflects static thermal exposure without concurrent mechanical loading.

3. Results

3.1. Initial Microstructures

Figure 2 shows SEM images of the two experimental steels. FR1 steel exhibited a mixed microstructure consisting of polygonal ferrite (PF) and granular bainite (GB) microstructure with phase fractions of approximately 55 vol% PF and 45 vol% GB (Figure 2a). Additionally, some fine particles can be observed in both the PF and bainitic ferrite (BF) matrix of FR1 steel, as indicated by the red arrows in Figure 2b, these particles will be further analyzed by TEM. During air cooling of FR1 steel, austenite first transforms into PF through diffusion mechanisms, accompanied by long-range diffusion of carbon from ferrite to the untransformed austenite, thereby lowering the transformation temperature of austenite to bainite [20,21]. This combination of increased carbon content and decreased transformation temperature resulted in the refinement of both BF and martensite/austenite (M/A) islands in the FR1 sample. By contrast, FR3 steel with high Mo content (0.5 wt.%) primarily consisted of GB and a small quantity of PF (approximately 10 vol.%), as marked by the black arrows in Figure 2c. It is well established that Mo suppresses the ferrite or pearlite transformation and significantly promotes the formation of bainite. Notably, the particles observed in FR1 were not found in FR3 steel (Figure 2d). Meanwhile, retained austenite (RA) is barely detected by XRD in both steel samples.

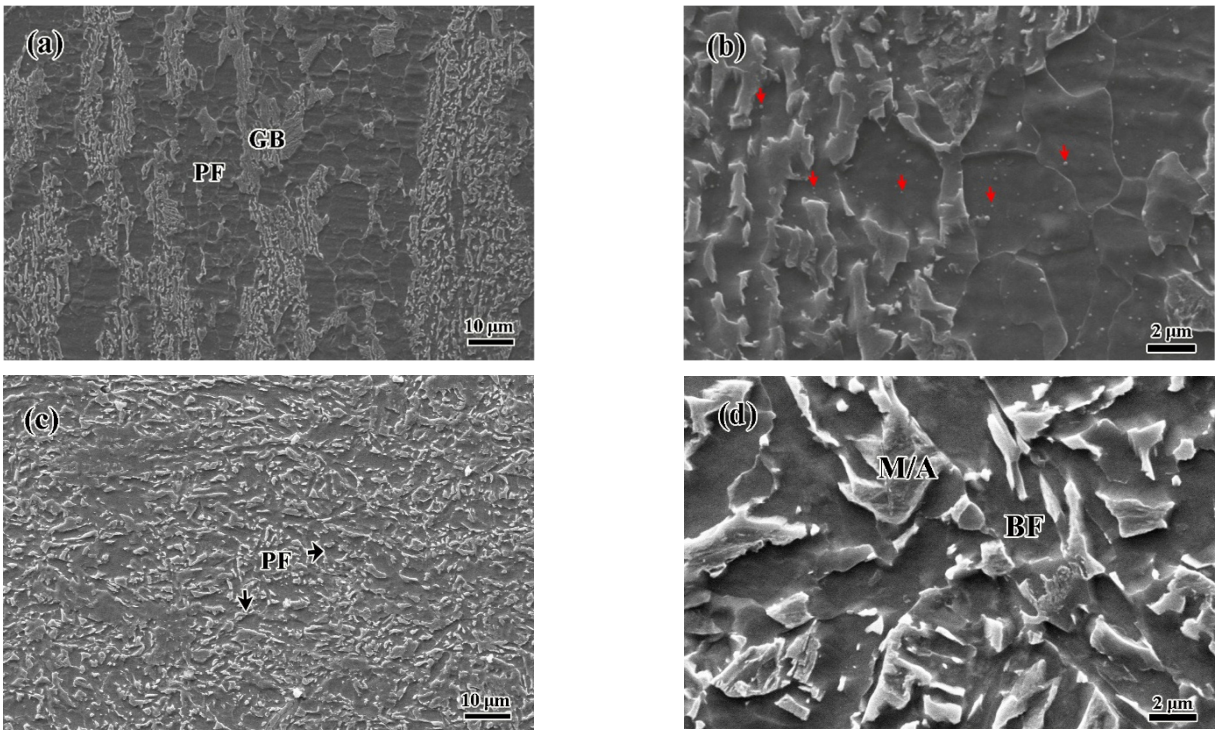

Figure 2. Microstructures of FR1 steel (**a**,**b**) and FR3 steel (**c**,**d**) after hot rolled and air cooling processes. PF: polygonal ferrite, GB: granular bainite. M/A: martensite/austenite, BF: bainitic ferrite.

Figure 3 presents detailed TEM and EDS characterizations of microstructures of the two experimental steels. It indicates that the dislocation density in PF (Figure 3a) is significantly lower than in the GB region (Figure 3b) in FR1 steel. Spherical precipitates approximately 100 nm in size are distributed within the PF matrix (Figure 3a). EDS analysis (Figure 3c) confirms that these precipitates are enriched in C, Nb, Ti, and Mo, indicating the formation of (Nb, Ti, Mo)C carbides. The atom fractions show high Nb and Ti content but relatively low Mo content in these precipitates. Previous studies report that Mo can enter the NbC or TiC lattice to replace some Nb or Ti atoms [22]. These carbides appear in both PF and bainitic ferrite (BF) matrices (Figure 2b), suggesting that they likely precipitated from parent austenite during hot rolling due to deformation-induced precipitation [23]. In contrast to the low dislocation density in PF, the BF in FR3 steel exhibited much higher dislocation density (Figure 3e). The high-density dislocation in GB results from transformation strain during the formation of BF and M/A [24]. No coarse carbide particle was observed in the as-hot-rolled microstructure of FR3 steel. Instead, spherical nano-precipitates ~15 nm in size are occasionally observed in the BF matrix.

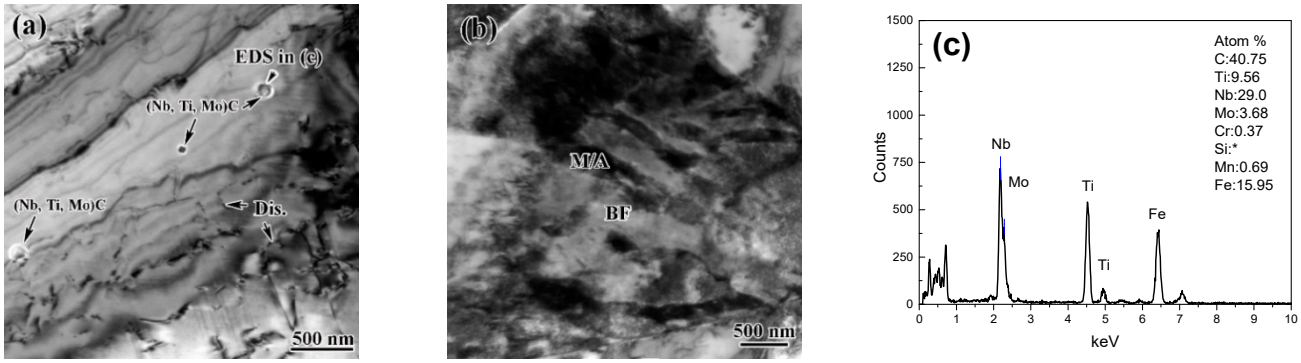

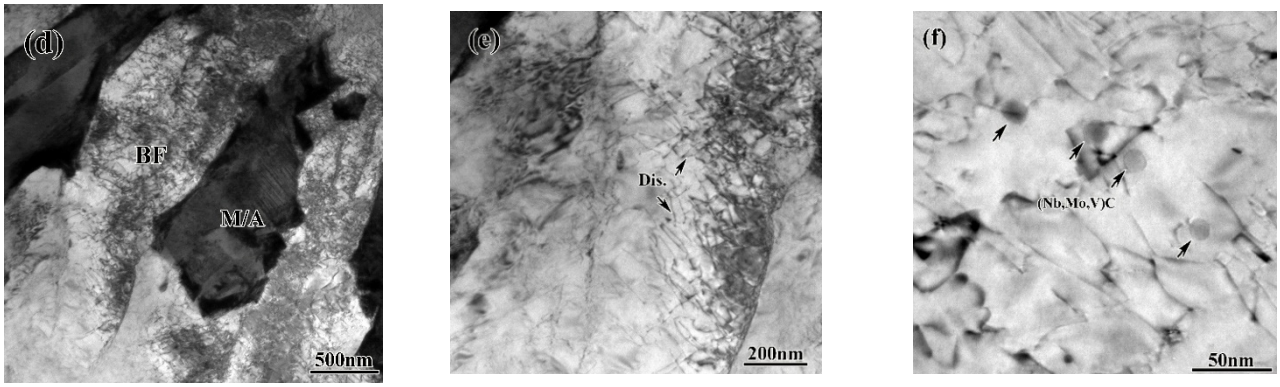

Figure 3. TEM and EDS results of microstructure in FR1 steel (**a**–**c**) and FR3 steel (**d**–**f**). M/A: martensite/austenite, BF: bainitic ferrite, Dis.: dislocation. *: Elements not detected by EDS.

3.2. Mechanical Properties

The tensile tests were performed on both steels in the hot-rolled samples and after thermal exposures at 600 °C for 3 h and 6 h, as shown in Table 2. The hot-rolled FR1 steel exhibited a yield strength (YS) of 464 MPa and an elongation of 25.6% at room temperature. Notably, thermal exposure at 600 °C caused severe degradation of strength. The YS of FR1 steel decreased to 246 MPa (47% reduction *vs.* RT) after 3 h exposure and to 282 MPa after 6 h exposure, which failed to meet the requirements of fire-resistant steel. However, FR3 steel with 0.5 wt.% Mo delivered superior room-temperature strength with the YS of 627 MPa and UTS of 985 MPa, which were about 35% and 27% higher than FR1 steel, respectively. The high room-temperature strength is mainly attributed to dislocation strengthening from its high-volume fraction of GB. After exposure at 600 °C, FR3 maintained excellent YS of 420 MPa (for 3 h) and 440 MPa (for 6 h), representing above 66.7% retention of room temperature YS with compliance to fire-resistant criteria. The limited 1/3 strength reduction in FR3 steel contrasted starkly with the catastrophic softening of FR1 steel, confirming the great benefit of the higher-Mo/lower-Cr alloy design in promoting high-temperature mechanical properties.

Table 2. Mechanical properties of test steels at room temperature and 600 °C.

Sample	Room Temperature			600 °C × 3 h		600 °C × 6 h	
	YS (MPa)	TS (MPa)	EI (%)	YS (MPa)	TS (MPa)	YS (MPa)	TS (MPa)
FR1	464 ± 19	804 ± 20	25.6 ± 0.7	246 ± 6	260 ± 12	282 ± 8	324 ± 5
FR3	627 ± 2	985 ± 7	18.9 ± 0.7	420 ± 8	472 ± 1	440 ± 17	479 ± 15

Note: YS—yield strength, TS—tensile strength, EI—total elongation. At least four specimens were prepared per condition; after excluding specimens that failed outside the gauge section, three valid replicates were obtained. Values are mean ± standard deviation.

3.3. Microstructures After Exposure at 600 °C for 3 h and 6 h

Figure 4 presents the SEM micrographs of both experimental steels after thermal exposure at 600 °C for 3 h and 6 h. After exposure at 600 °C for 3 h (Figure 4a,b), the GB in FR1 steel underwent significant decomposition, accompanied by carbide precipitation along lath boundaries and prior austenite grain boundaries. When the exposure time is extended to 6 h (Figure 4c,d), lath recovery occurs within the GB areas of FR1, where M/A islands become less distinct. Notably, PF maintains a stable morphology without significant coarsening throughout the 3–6 h exposures at 600 °C, confirming that the PF grains do not undergo substantial growth at elevated temperature. In contrast, for the FR3 steel, although the M/A islands in the GB region decompose extensively into ferrite and carbides after exposure at 600 °C, the overall morphology of GB remains clearly distinguishable even after 6 h (Figure 4g,h).

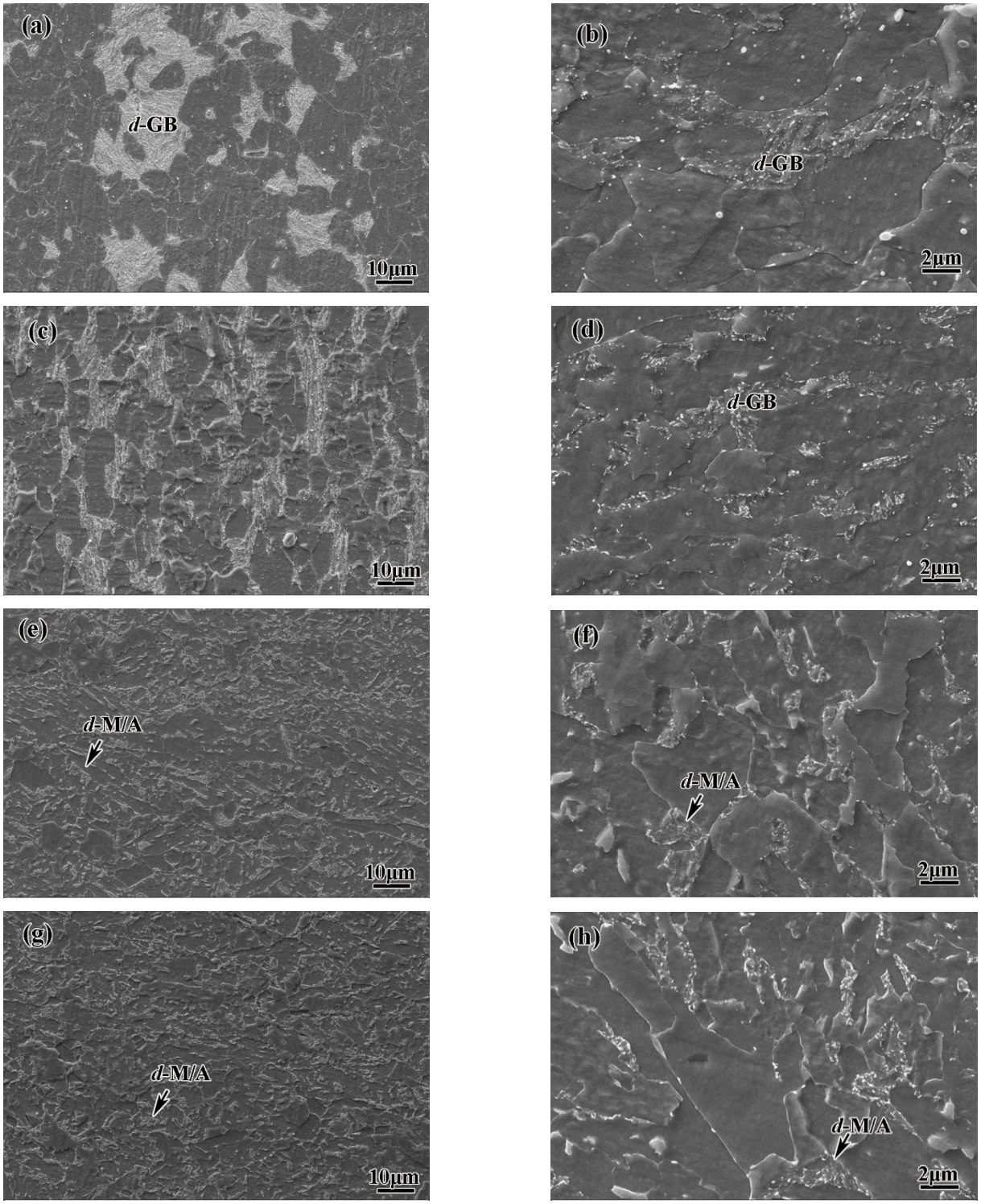

Figure 4. Microstructure after exposure at 600 °C for 3 h (**a**,**b**) and 6 h (**c**,**d**) of FR1 steel and 3 h (**e**,**f**) and 6 h (**g**,**h**) of FR3 steel. d-GB: decomposed granular bainite, d-M/A: decomposed M/A island.

Figure 5 presents TEM and EDS results of FR1 samples after thermal exposure at 600 °C for 3 h and 6 h. Microstructural analysis indicates that after 3 h thermal exposure, spherical/rod-shaped carbides preferentially precipitate along prior austenite grain boundaries (PAGBs) and lath boundaries within GB (as marked by red arrows in Figure 5a). EDS results in Figure 5b demonstrate that the coarse carbide precipitated in PF are (Nb, Ti, Mo) C, similar to those observed in the rolled state. In contrast, the carbides precipitated along the GB/PF interface are enriched in Cr and Mn, as shown in Figure 5c. It has been

reported that Cr and Mn partition into cementite during high temperature tempering, thereby retarding its coarsening rate [25]. The lath boundaries of BF remain discernible after 3 h of exposure, despite the precipitation of the slender-shaped carbides along these lath boundaries (Figure 5d). Bright-field imaging and selected-area diffraction in Figure 5e confirm that the spherical/rod-shaped carbides at lath boundaries are cementite. Owing to the faster diffusion rate of carbon, cementite is likely to form first along lath boundaries. With prolonged thermal exposure time, M_7C_3 or $M_{23}C_6$ carbides may subsequently develop due to continued enrichment of alloying elements such as Mn and Cr [26].

After 6 h of thermal exposure, equiaxed ferrite grains with dispersed spherical or short-rod carbides are observed (Figure 5f), which are formed through the recrystallization process [27]. During thermal exposure, the stored deformation energy accumulated from prior hot rolling drives static recovery processes involving dislocation rearrangement and annihilation. With extended exposure time, dislocations tend to organize into two-dimensional sub-grain walls, and partial recrystallization may occur in regions with sufficiently high stored energy. With extended exposure time, dislocations tend to organize two-dimensional sub-grain walls [28], as shown in Figure 5g. The recrystallized regions contain three types of carbides: spherical and short-rod carbides predominantly along subgrain boundaries, nano-sized spherical carbides within equiaxed ferrite grains (Figure 5f). Bright-field/dark-field TEM images and selected-area diffraction (Figure 5h,i) confirm the formation of M_7C_3 carbide. Previous studies indicate that the more stable M_7C_3 can partially replace M_3C cementite during prolonged high-temperature tempering [29]. These observations agree with Thermo-Calc predictions, which identify three equilibrium carbide types (MC, M_7C_3, and $M_{23}C_6$) at 600 °C in FR1 steel.

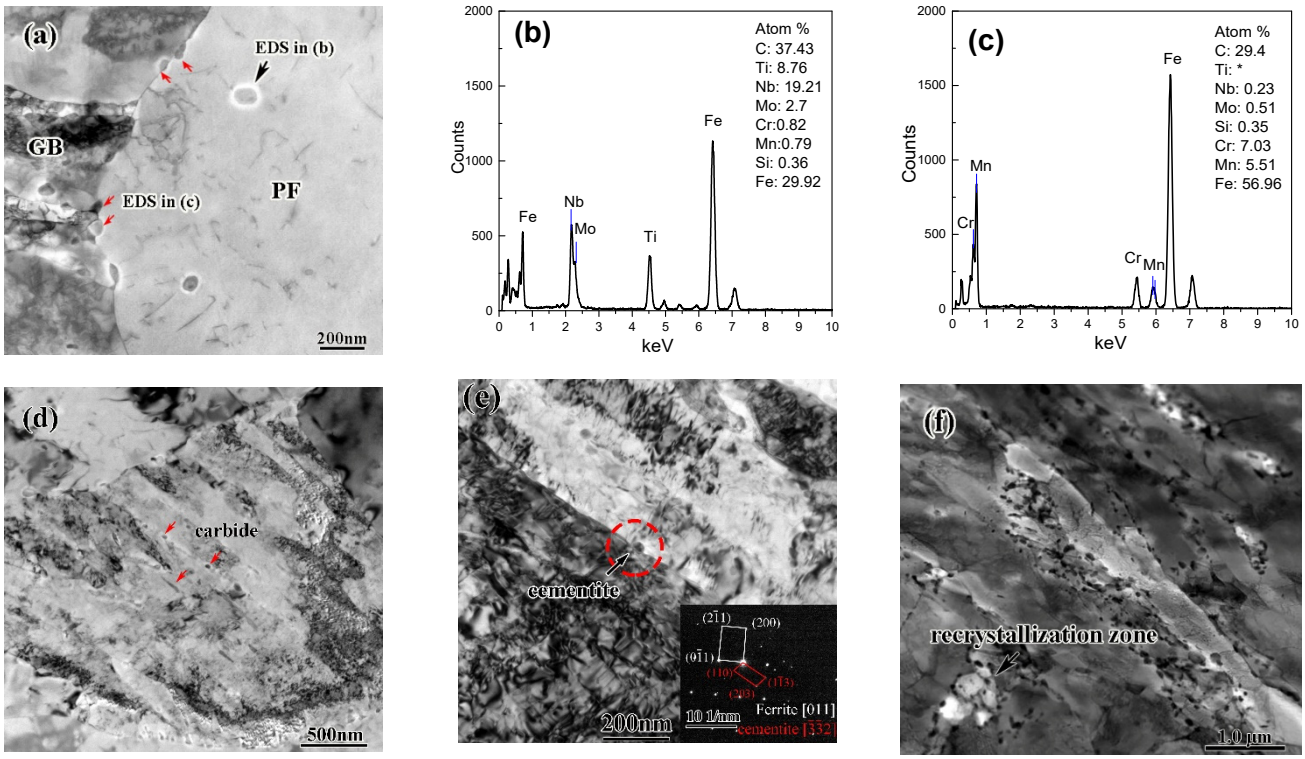

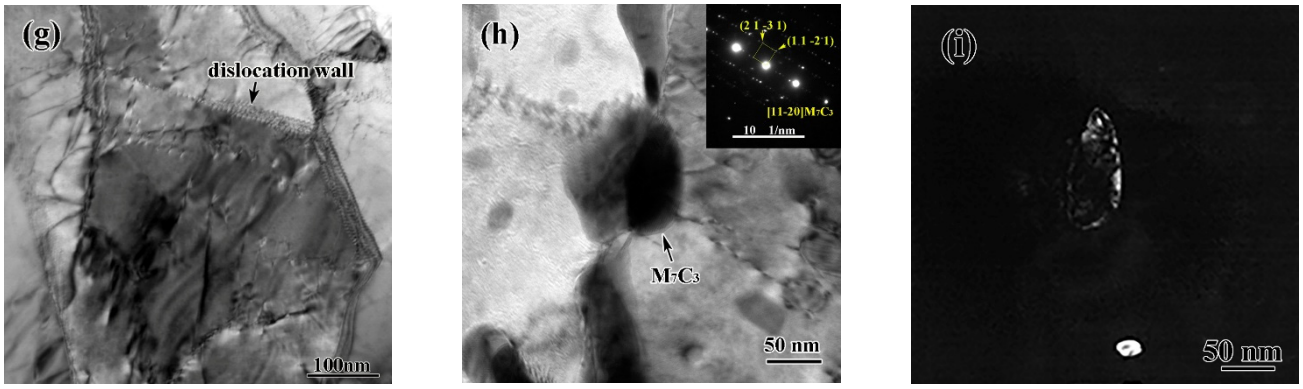

Figure 5. Evolution of microstructure characterized by TEM of FR1 steel after exposure at 600 °C for 3 h (**a**–**e**) and 6 h (**f**–**i**). GB: granular bainite, PF: polygonal ferrite. *: Elements not detected by EDS.

Figure 6 presents microstructural evolution of the FR3 steel after thermal exposure at 600 °C, as characterized by TEM and EDS. After 3 h of exposure, BF lath boundaries remain visible, with the slender-shaped carbides precipitating along BF lath boundaries or at the interfaces of BF and M/A (Figure 6a). The EDS analysis in Figure 6b indicates that the carbides are enriched in Cr and Mn. Meanwhile, EDS analysis of carbon extraction replicas reveals the presence of nano-scale (Nb, Mo, V)C carbides (~20 nm in size) within BF laths (Figure 6c–e), suggesting that these nano-sized precipitates were newly formed in the BF matrix during exposure at 600 °C.

After 6 h of exposure at 600 °C, the FR3 steel retains a well-defined morphology of GB despite significant decomposition of the M/A islands (Figure 6f). Notably, the dislocation density within the BF laths remains very high (Figure 6g). The bright and dark-field TEM images and selected-area diffraction patterns in Figure 6h–i reveal numerous nano-sized MC precipitates with a size of ~20 nm distributed in BF matrix. The EDS spectrum in Figure 6k confirms that these precipitates are enriched in C, Nb, Mo, and V, thereby identifying them as (Nb, Mo, V)C carbides. In Nb–Mo steels, when Nb carbides precipitate in BF, Mo atoms tend to substitute into the NbC lattice by replacing partial Nb atoms, forming (Nb, Mo)C. This substitution reduces the interfacial energy between the carbide and the ferrite matrix, thereby decreasing the nucleation energy barrier. As a result, Mo addition promotes Nb precipitation and increases the nucleation density [30]. These nano-sized (Nb, Mo, V)C carbides can pin the dislocations and hinder their movement during thermal exposure (Figure 6j). Hence, the integrity of BF lath is preserved, without obvious recrystallization. Compared to the sample exposed for 3 h, the carbides along the interfaces between M/A and BF undergo spheroidization after prolonged exposure for 6 h, transitioning from slender-shape to spherical or rod-shape (Figure 6a,l). Meanwhile, the carbides in FR3 steel are notably finer than those in FR1 steel (as indicated by black arrows in Figure 6l). Both experimental steels underwent identical rolling processes and have the same carbon content, although they differ in both Mo and Cr contents (FR1: 0.25 wt.% Mo/1.19 wt.% Cr; FR3: 0.50 wt.% Mo/0.81 wt.% Cr). Their carbide precipitation sequences are nevertheless expected to be broadly similar: initial cementite formation followed by diffusion of alloying elements to form M7C3 or M23C6. Nevertheless, a distinct difference in carbide size is observed between the two steels, which will be discussed in detail subsequently.

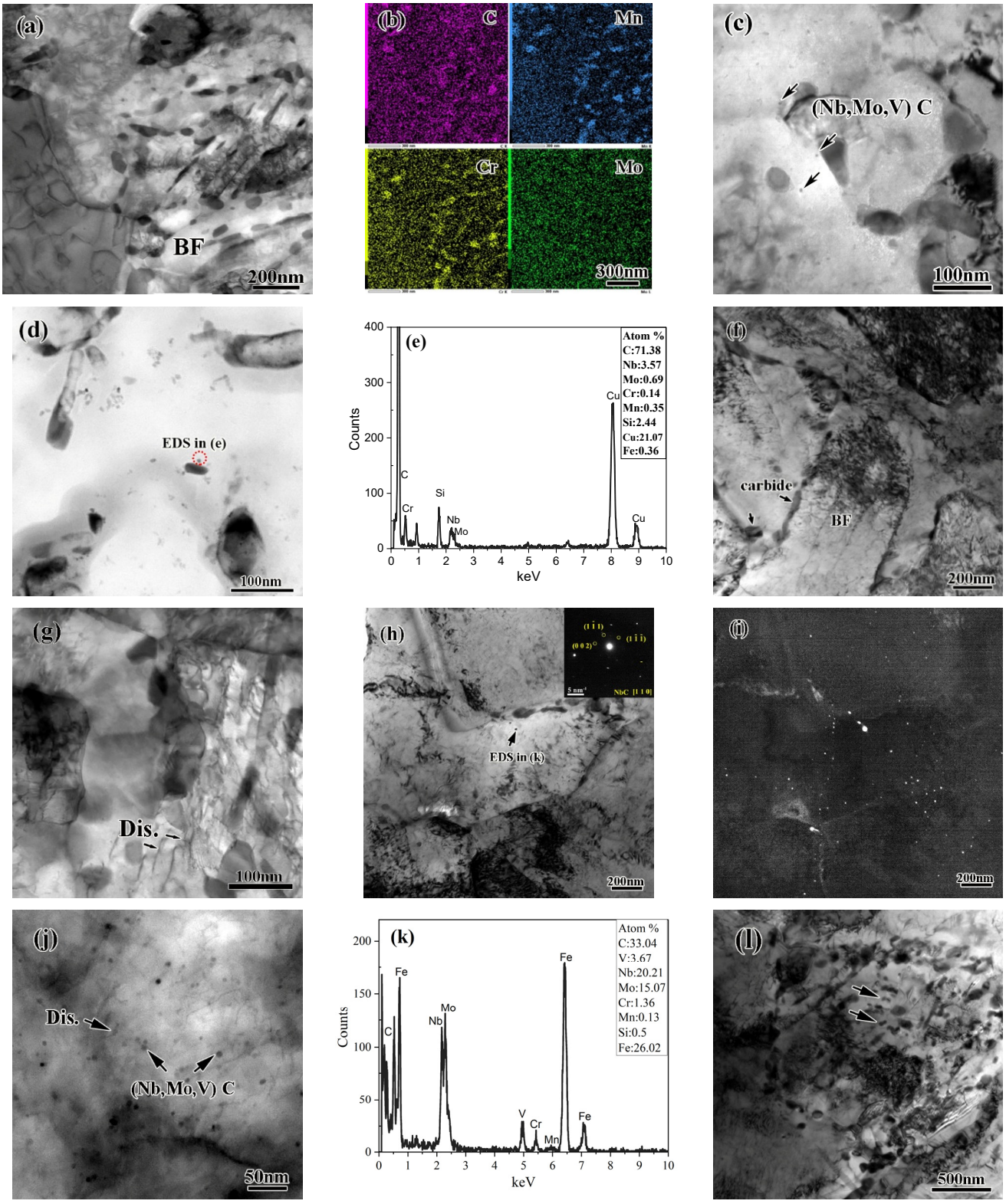

Figure 6. TEM and EDS results showing microstructural evolutions of FR3 steel exposed at 600 °C for 3 h (**a**–**e**) and 6 h (**f**–**l**). EDS analysis of (Nb, Mo, V)C precipitates as marked by the red dotted box of FR3 steel exposed at 600 °C for 3 h (**e**) and (Nb, Mo, V,)C precipitates as marked by the black arrow of FR3 steel exposed at 600 °C for 6 h (**k**). BF: bainitic ferrite, Dis.: dislocation.

4. Discussion

4.1. Thermal Stability of Microstructures

To elucidate the difference in microstructural evolution between the two experimental steels at 600 °C, EBSD analysis was conducted following various high-temperature durations. Figure 7 presents EBSD results for FR1 steel before exposure and after 3 h and 6 h exposure at 600 °C, presenting band contrast (BC) maps, grain boundary maps, and Kernel average misorientation (KAM) maps. Typically, in EBSD images, high dislocation densities correspond to low BC [31]. The PF phase exhibits high BC, while regions with low BC correspond to GB areas. Results indicate that after 3 h exposure, the GB volume fraction remains similar to the initial state but decreases sharply after 6 h exposure (~27.6 vol.%). The effective grain sizes (with high-angle boundaries, misorientation ≥ 15°) of FR1 specimens in the three states measure 3.29 μm, 3.63 μm, and 2.62 μm respectively, indicating grain refinement after 6 h exposure. The PF grain size statistics in FR1 steel reveal a hot-rolled state, and 600 °C/3 h exposed specimens exhibit grain sizes of 4.6 μm and 4.21 μm (equivalent circle diameter), respectively. After 600 °C/6 h exposure (Figure 7c), the equiaxed ferrite grains (1–2 μm) emerged, with overall PF grain size decreasing to 2.12 μm. This demonstrates partial recrystallization of GB in FR1 steel after 600 °C/6 h exposure. Generally, KAM values represent local lattice curvature and distortion levels, where high KAM correlates with high crystal defect densities such as dislocations [32,33]. Compared to PF, GB regions exhibit significantly higher KAM values, indicating high dislocation densities in GB regions. Dislocation density can be determined from KAM values [34] as follows:

$$\rho = 2\theta/\mu b \quad (1)$$

where ρ is the dislocation density, θ is the average KAM value, μ is the EBSD step size, and b is the Burgers vector. The dislocation density in the hot-rolled FR1 specimen is ~9.35×10^{14} m^{-2} for GB and ~1.6×10^{14} m^{-2} for PF. After 3 h/6 h thermal exposure, the dislocation density of non-recrystallized GB area decreased to ~8.45×10^{14} m^{-2} and ~5.97×10^{14} m^{-2}, respectively, while that of PF remained stable (~1.2×10^{14} m^{-2} and ~1.3×10^{14} m^{-2}). Concurrently, average dislocation density decreases from ~4.1×10^{14} m^{-2} (hot-rolled) to ~3.5×10^{14} m^{-2} (exposure for 3 h) and ~2.7×10^{14} m^{-2} (exposure for 6 h). These results demonstrate rapid GB decomposition in the FR1 specimen during 6 h exposure, indicating inadequate durability for long-term high-temperature service.

Figure 8 displays EBSD maps of FR3 steel in the hot-rolled state and after 600 °C thermal exposure for 3 h and 6 h, including band contrast (BC), grain boundary maps, and Kernel average misorientation (KAM) maps. The PF regions exhibit significantly lower KAM values (Figure 8a). KAM maps confirm the SEM results, revealing that there was approximately 12 vol.% PF in air-cooled FR3 steel after hot rolling. After exposure, the PF content and size have remained basically unchanged. The effective grain sizes (high-angle boundaries, misorientation ≥ 15°) of FR3 specimens under three conditions measure 3.13 μm, 3.03 μm, and 3.59 μm respectively, demonstrating negligible variation in effective grain size during 600 °C exposure. Geometrically necessary dislocation (GND) densities calculated for as-rolled, 3 h-exposed, and 6 h-exposed conditions remain stable at 7.2×10^{14} m^{-2}, 6.81×10^{14} m^{-2}, and 7.16×10^{14} m^{-2}. The evolution trends of substructure and dislocations with exposure time indicate superior thermal stability in FR3 steel.

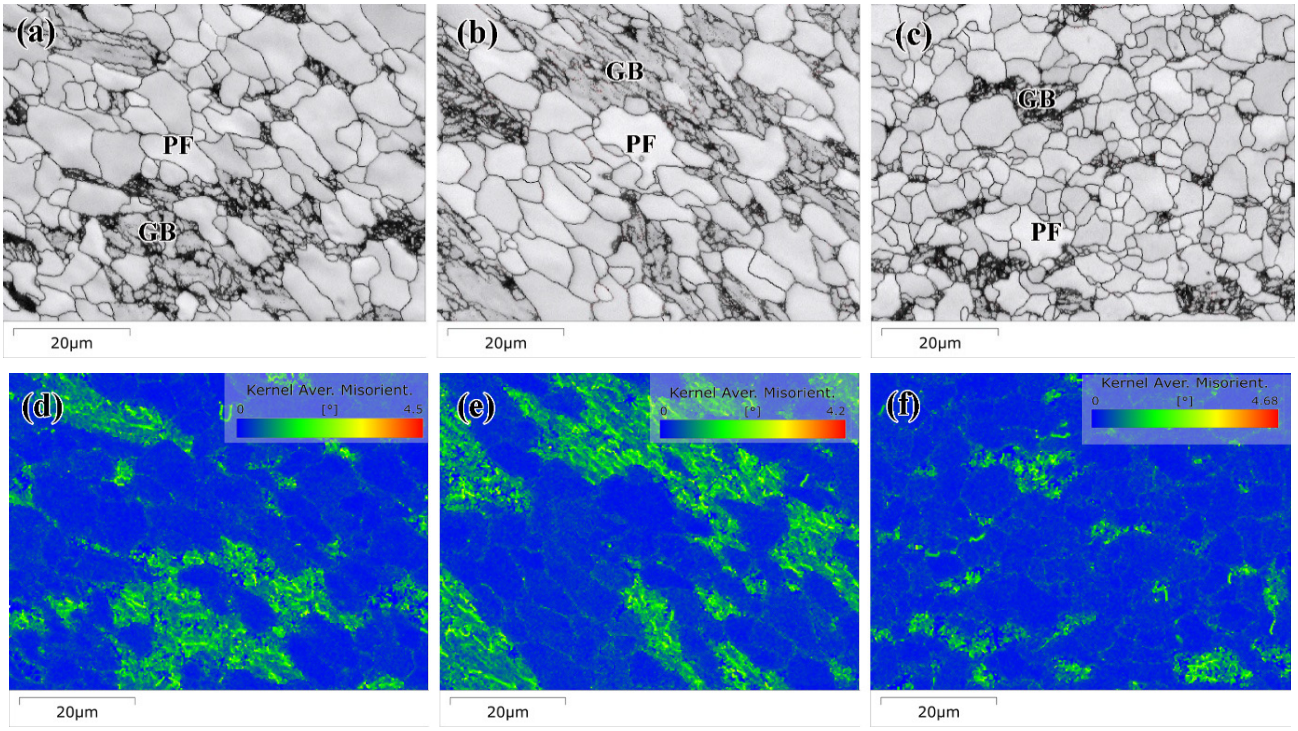

Figure 7. EBSD results of FR1 steel before exposure (**a**,**d**) and after exposure at 600 °C for 3 h (**b**,**e**) and for 6 h (**c**,**f**). (**a**–**c**) combined BC and grain boundary, thick grey lines: high angle boundary with misorientation > 15°, thin grey lines: low angle boundary with misorientation of 2–15°; (**d**–**f**) KAM maps.

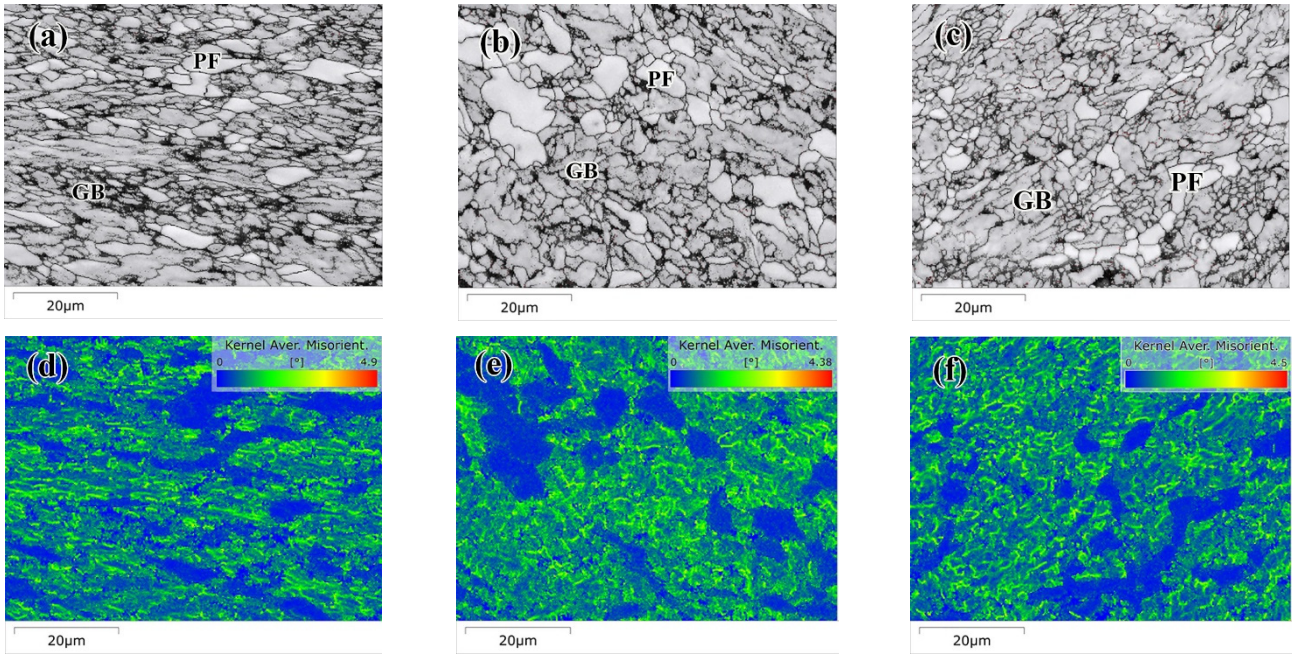

Figure 8. EBSD results of FR3 steel before exposure (**a**,**d**) and after exposure at 600 °C for 3 h (**b**,**e**) and for 6 h (**c**,**f**). (**a**–**c**) combined BC and grain boundary, thick grey lines: high angle boundary with misorientation > 15°, thin grey lines: low angle boundary with misorientation of 2–15°; (**d**–**f**) KAM maps.

4.2. Precipitation Behavior and Strengthening Mechanisms

APT characterization was performed on specimens exposed at 600 °C for 6 h to resolve the finest-scale MC carbides and clusters (Figures 9 and 10). For comparison, TEM-based quantitative statistics on carbide sizes for both 3 h and 6 h conditions are summarized in Table 3. The analyzed volume of the APT tip is

approximately 5.58×10^5 nm^3, estimated from the dataset dimensions. Figure 9a shows 3D atom reconstruction maps of Fe, Si, Cr, Mn, Nb, Mo, Ti, and C for FR1 steel after 6 h at 600 °C. The uneven distributions of Cr, Mn, Mo, Ti, and C are evident. Although Nb-rich carbides were observed in the 600 °C/6 h exposed FR1 steel, they were not detected via APT in the selected needle region. Therefore, iso-concentration surfaces at 2 at.% C, 2 at.% Cr, 3.8 at.% Mn, 0.7 at.% Mo, and 0.3 at.% Ti was utilized to reconstruct the 3D atom maps, as shown in Figure 9b. A coarse carbide with a size of ~30 nm is observed (marked by arrows), enriched in Cr and Mn. The proxigram in Figure 9b1 reveals that C, Mn, and Cr contents reach 12 at.%, 20 at.%, and 14 at.%, respectively, suggesting the carbide is likely $M_{23}C_6$. In contrast, Mo tends to coexist with Ti, forming nano-sized fine (Ti, Mo)C precipitates or Ti/Mo-enriched clusters, as shown in Figure 9c. Quantitative statistical analysis identified 21 such clusters, corresponding to a number density of $(3.76 \pm 0.3) \times 10^{22}$ m^{-3} with an average size of 3.97 ± 1.16 nm. It is reported that Mo tends to replace Ti during the initial stage of TiC precipitation from either austenite [35] or ferrite [22]. The replacement of Ti by Mo decreases the interfacial chemical energy of MC/austenite system or decreases the misfit between MC and ferrite, which accelerates the early precipitation of (Ti, Mo)C.

Figure 10 presents 3D atom reconstruction maps of Fe, Si, Cr, Mn, Nb, Mo, V, and C in the GB region of FR3 steel after 6 h at 600 °C. Fe, Si, Cr, and Mn exhibit uniform distributions, while Nb, Mo, V, and C show varying degrees of enrichment. Figure 10b displays 3D reconstructions using iso-concentration surfaces at 2.5 at.% C, 2.1 at.% Mo, 0.5 at.% Nb, and 0.7 at.% V. Significant spatial coincidence is observed among the enrichment zones of C, Nb, Mo, and V. Sites 1 and 2 in Figure 10b (size ~10 nm) exhibit Nb, Mo, and V contents of 30–40 at.%, 10–15 at.%, and 1–5 at.%, corresponding to (Nb, Mo, V)C carbides. In Region 3 (Figure 10b), nanoparticles (<5 nm) aligned in a near-matrix configuration contain ~10–20 at.% C, 5–10 at.% Nb and Mo, and <5 at.% V, likely representing dislocation-associated clusters. Quantitative APT statistics reveal that the number density of these (Nb, Mo, V)C carbides is $(5.37 \pm 0.6) \times 10^{21}$ m^{-3}, with an average size of 10.3 ± 2.7 nm. Region 4 contains randomly distributed nanoparticles with similar dimensions and chemistry to those in Region 3. The combined number density of clusters in Regions 3 and 4 reaches $(4.12 \pm 0.4) \times 10^{22}$ m^{-3}, with an average size of 4.29 ± 1.12 nm.

A comparison of the APT data reveals that the number density of nano-clusters in FR3 (4.12×10^{22} m^{-3}) is similar, within the analysed APT volumes, to that in FR1 (3.76×10^{22} m^{-3}), differing by less than 10%. However, Table 2 shows that after 6 h at 600 °C, the yield strength of FR3 (~440 MPa) exceeds that of FR1 (~282 MPa) by 158 MPa. This significant mechanical disparity, despite the near-identical precipitate densities, implies that precipitation strengthening alone cannot account for the enhanced performance of FR3. Instead, the drastic difference in GB fraction (88 vol.% in FR3 *vs.* 45 vol.% in FR1) and the associated microstructural stability are the dominant factors.

The compositional differences between the steels significantly affect carbide coarsening kinetics. Table 3 compares carbide sizes after 6 h at 600 °C. The spherical carbides in FR3 (63 nm) are considerably finer than those in FR1 (112 nm). This can be attributed to two primary factors. Firstly, the formation of ~55% PF during air-cooling in FR1 enriches carbon in the untransformed austenite, resulting in a carbon content of up to 0.24 wt.% within the GB regions—twice the nominal alloy content (~0.12 wt.%). In contrast, only ~12% PF forms in FR3, leading to milder carbon enrichment in the GB regions. The combination of carbon enrichment (~0.24 wt.%) and high initial dislocation density ($\sim 9.35 \times 10^{14}$ m^{-2}) in FR1 accelerates carbide coarsening via enhanced pipe diffusion [36]. Secondly, the decomposition of M/A islands in both steels promotes cementite formation. Over time, Mn and Cr diffuse into the cementite, facilitating its transformation to M_7C_3or $M_{23}C_6$ [37,38]. The higher Mo content in FR3 (0.50 wt.%) effectively retards this coarsening process. Mo partitions preferentially to these carbides and exerts a solute-drag effect that hinders the diffusion of substitutional elements, thereby stabilizing the fine precipitate distribution [39,40].

In summary, FR3 steel exhibits superior high-temperature performance due to a synergistic effect: the moderate initial dislocation density within the GB matrix provides abundant nucleation sites for precipitates,

while the increased Mo and reduced Cr content effectively suppress carbide coarsening. The resulting fine and dense dispersion of (Nb, Mo, V)C carbides and Mo–Nb-rich clusters effectively pins dislocations and retards the recovery process. This mechanism preserves the integrity of the GB matrix, which acts as the primary load-bearing constituent at elevated temperatures [41]. Recent empirical modeling by Park et al. [42] relates the 600 °C yield strength to the initial bainite fraction (VB): YS600 °C =2.4130 × VB + 175.86. Applying this model to FR1 (VB ≈ 45%) and FR3 (VB ≈ 88%) yields predicted strengths of 284.4 MPa and 388.0 MPa, respectively. These values align well with the experimental measurements (within a 15% margin), reinforcing that dislocation strengthening and precipitation strengthening, governed by the GB fraction and carbide dispersion, constitute the core mechanisms for fire-resistant steels. Through optimized alloy design balancing Mo and Cr, the present study achieves a 600 °C yield strength of 440 MPa and a YS600 °C/YSRTratio of ~0.67, meeting the criteria for long-duration fire resistance. It should be noted that Mo and Cr were varied simultaneously in the present alloy design; therefore, the results demonstrate the superiority of the combined higher-Mo/lower-Cr concept for long-term fire resistance, but do not completely isolate the independent contribution of Mo.

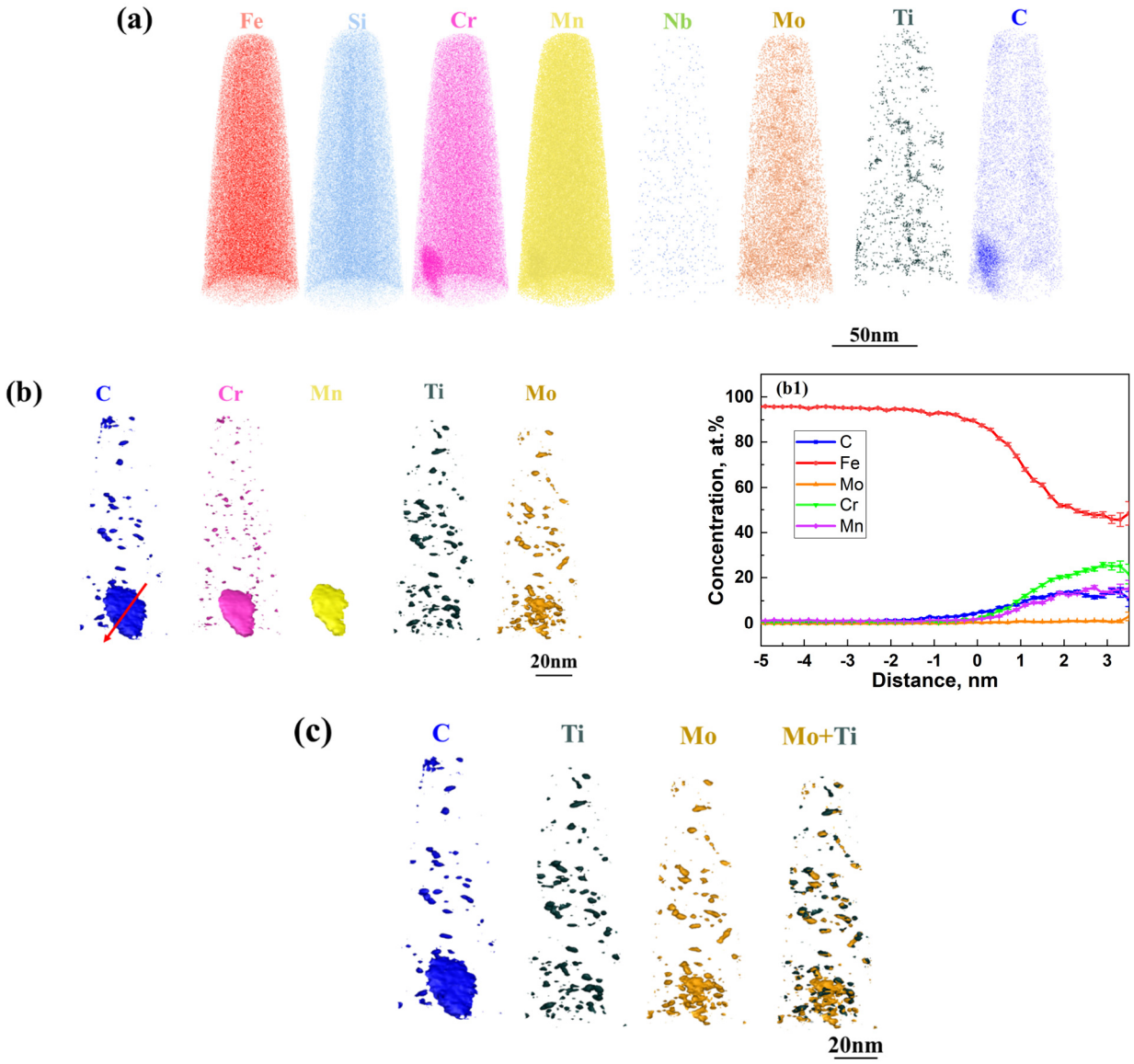

Figure 9. 3D−APT reconstruction maps of FR1steel. (**a**) Fe, Si, Cr, Mn, Nb, Mo, C element; (**b**) Iso-concentration surfaces of 2 at.%C, 0.7 at.%Mo, 2 at.%Cr, 3.8 at.%Mn and 3 at.% Ti maps; (**b1**) Proximity histogram based on ICS in (**b**); (**c**) Iso-concentration surfaces of 2 at.%C, 3 at.% Ti, 0.7 at.%Mo and 3 at.% Ti + 0.7 at.%Mo maps.

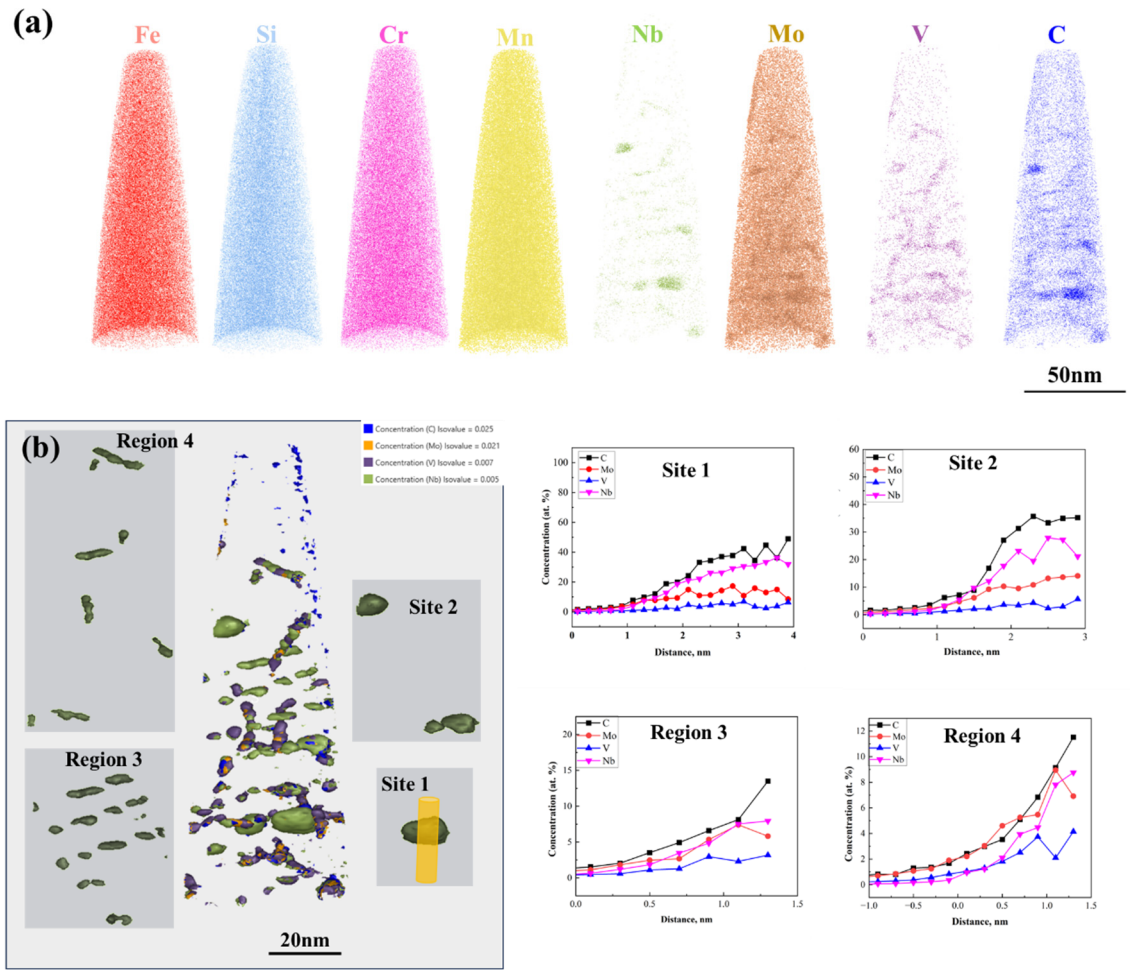

Figure 10. 3D-APT reconstruction maps of FR3 steel. (**a**) Fe, Si, Cr, Mn, Nb, Mo, V, C element; (**b**) Iso-concentration surfaces of 2.5 at.%C, 2.1 at.%Mo, 0.5 at.%Nb, 0.7 at.%V maps.

Table 3. Size of precipitates of tested steels exposed at 600 °C for different times.

Carbide	FR1-3 h	FR1-6 h	FR3-3 h	FR3-6 h
Carbide-sphere	84 ± 25	112 ± 24	46.6 ± 15	63 ± 17
Carbide-short-rod (length/width)	82 ± 15/30 ± 9	143 ± 29/46 ± 13	63 ± 12/23 ± 6	74 ± 10/28 ± 7

5. Conclusions

In this study, two fire-resistant steels with different Mo contents were produced via hot rolling followed by air cooling. Detailed comparisons were made regarding their high-temperature strength and microstructural evolution after exposure at 600 °C for 3 h and 6 h. The main conclusions are as follows:

1. The FR3 steel (0.5 wt.% Mo) exhibits excellent mechanical properties after hot rolling and air cooling, achieving a tensile strength of 985 MPa and a yield strength of 627 MPa at room temperature—significantly higher than those of the FR1 steel (0.25 wt.% Mo), which has a yield strength of 464 MPa. After thermal exposure at 600 °C for 6 h, the yield strength of FR3 steel remains as high as 440 MPa, meeting the fire-resistant steel requirement and substantially outperforming FR1 steel (only 282 MPa under the same conditions).
2. Increasing the Mo content from 0.25 wt.% to 0.5 wt.% (with a concomitant reduction in Cr from 1.2 wt.% to 0.8 wt.%) nearly doubles the fraction of granular bainite (from ~45% to ~88%) and enhances its high-temperature stability. The higher Mo content also suppresses the precipitation of NbC in the parent austenite, thereby promoting the formation of nanosized MC carbides within the bainitic ferrite during thermal exposure, which provides effective precipitation strengthening. The increased fraction

of granular bainite, its superior thermal stability, and the nanoscale precipitation collectively account for the excellent long-term fire resistance of the FR3 steel.

Acknowledgments

The authors gratefully acknowledge the funding from CNPC Scientific Research and Technology Development Project (2021ZZ03, 2023ZZ11, 2022DQ03-02 & 2020B-4020).

Author Contributions

Conceptualization, C.F. and G.G.; Methodology, X.G.; Formal Analysis, L.Z. and X.G.; Investigation, L.Z.; Resources, C.F. and L.Z.; Data Curation, X.G.; Writing—Original Draft Preparation, L.Z. and X.G.; Writing—Review & Editing, L.Z. and X.G.; Supervision, C.F.; Project Administration, Q.J.

Ethics Statement

Not applicable.

Informed Consent Statement

Not applicable.

Data Availability Statement

Data will be made available on request.

Funding

This research was funded by CNPC Scientific Research and Technology Development Project grant number 2021ZZ03, 2023ZZ11, 2022DQ03-02 and 2020B-4020.

Declaration of Competing Interest

The authors declare that they have no known competing financial interests or personal relationships that could have appeared to influence the work reported in this paper.

References

1. Sha W, Kelly FS, Browne P, Blackmore SPO, Long AE. Development of structural steels with re resistant microstructures. *Mater. Sci. Technol.* **2002**, *18*, 319–325. DOI:10.1179/026708301225000789
2. Sakumoto Y, Yamaguchi T, Ohashi M, Saito H. High-Temperature Properties of Fire-Resistant Steel for Buildings. *J. Struct. Eng.* **1992**, *118*, 392–407. DOI:10.1061/(ASCE)0733-9445(1992)118:2(392)
3. Morozov YD, Chevskaya ON, Filippov GA, Muratov AN. Fire-resistant structural steels. *Metallurgist* **2007**, *51*, 356–366. DOI:10.1007/s11015-007-0067-4
4. Sha W, Kelly FS, Guo ZX. Microstructure and properties of nippon fire-resistant steels. *J. Mater. Eng. Perform.* **1999**, *8*, 606–612. DOI:10.1007/s11665-999-0017-3
5. Wang W, Zhang Y, Xu L, Li X. Mechanical properties of high-strength Q960 steel at elevated temperature. *Fire Saf. J.* **2020**, *114*, 103010. DOI:10.1016/j.firesaf.2020.103010
6. Assefpour-Dezfuly M, Hugaas BA, Brownrigg A. Fire resistant high strength low alloy steels. *Mater. Sci. Technol.* **1990**, *6*, 1210–1214. DOI:10.1179/mst.1990.6.12.1210
7. Han G, Hu B, Yu YS, Rong XQ, Xie ZJ, Misra RDK, et al. Atomic-scale study on the mechanism of formation of reverted austenite and the behavior of Mo in a low carbon low alloy system. *Mater. Charact.* **2020**, *163*, 110269. DOI:10.1016/j.matchar.2020.110269
8. Lee WB, Hong SG, Park CG, Kim KH, Park SH. Influence of Mo on precipitation hardening in hot rolled HSLA steels containing Nb. *Scr. Mater.* **2000**, *43*, 319–324. DOI:10.1016/S1359-6462(00)00411-5

9. Lee WB, Hong SG, Park CG, Park SH. Carbide precipitation and high-temperature strength of hot-rolled high-strength, low-alloy steels containing Nb and Mo. *Metall. Mater. Trans. A* **2002**, *33*, 1689–1698. DOI:10.1007/s11661-002-0178-2
10. Wan R, Sun F, Zhang L, Shan A. Effect of Mo Addition on Strength of Fire-Resistant Steel at Elevated Temperature. *J. Mater. Eng. Perform.* **2014**, *23*, 2780–2786. DOI:10.1007/s11665-014-1051-3
11. Li Z, Zhang K, Wang W, Wang X, Cao Y, Yong Q. Mechanical Properties and Precipitation Behaviors of a Low-Mo Nb–V–Ti Complex Microalloyed Fire-Resistant Steel with Two Kinds of Microstructure. *Steel Res. Int.* **2022**, *93*, 2100515. DOI:10.1002/srin.202100515
12. Walp MS, Speer JG, Matlock DK. Fire-Resistant Steels for Construction Applications. In Proceedings of the 2003 AIST Steel Properties and Applications Conference, Indianapolis, IN, USA, 5–7 May 2003; pp. 123–132.
13. Wang X, Li Z, Zhou S, Wang W, Yong Q, Yang Z, et al. Precipitation behavior of Ti–Nb–V–Mo quaternary microalloyed high strength fire-resistant steel and its influence on mechanical properties. *Mater. Sci. Eng. A* **2021**, *807*, 140865. DOI:10.1016/j.msea.2021.140865
14. Fang HS, Feng C, Zheng YK, Yang ZG, Bai BZ. Creation of Air-Cooled Mn Series Bainitic Steels. *J. Iron Steel Res. Int.* **2008**, *15*, 1–9. DOI:10.1016/S1006-706X(08)60257-5
15. Cheng X, Gao G, Liu R, Gui X, Bai B, Feng C. Development of Air-Cooled Carbide-Free Bainite/Martensite Multiphase Steel: Transformation Kinetics, Microstructure, and Mechanical Properties. *Steel Res. Int.* **2024**, *95*, 2300619. DOI:10.1002/srin.202300619
16. Kyung Sung H, Ho Lee D, Yong Shin S, Lee S, Yong Yoo J, Hwang B. Effect of finish cooling temperature on microstructure and mechanical properties of high-strength bainitic steels containing Cr, Mo, and B. *Mater. Sci. Eng. A* **2015**, *624*, 14–22. DOI:10.1016/j.msea.2014.11.035
17. *GB/T 228.1-2021*; Metallic Materials—Tensile Testing—Part 1: Method of Test at Room Temperature. Standards Press of China: Beijing, China, 2021.
18. *GB/T 228.2-2015*; Metallic Materials—Tensile Testing—Part 2: Method of Test at Elevated Temperature. Standards Press of China: Beijing, China, 2015.
19. Wu YX, Sun WW, Gao X, Styles MJ, Arlazarov A, Hutchinson CR. The effect of alloying elements on cementite coarsening during martensite tempering. *Acta Mater.* **2020**, *183*, 418–437. DOI:10.1016/j.actamat.2019.11.040
20. Qiu C, Zurob HS, Panahi D, Brechet YJM, Purdy GR, Hutchinson CR. Quantifying the Solute Drag Effect on Ferrite Growth in Fe–C–X Alloys Using Controlled Decarburization Experiments. *Metall. Mater. Trans. A* **2013**, *44*, 3472–3483. DOI:10.1007/s11661-012-1547-0
21. Lan YJ, Li DZ, Li YY. Modeling austenite decomposition into ferrite at different cooling rate in low-carbon steel with cellular automaton method. *Acta Mater.* **2004**, *52*, 1721–1729. DOI:10.1016/j.actamat.2003.12.045
22. Jang JH, Lee CH, Heo YU, Suh DW. Stability of (Ti, M)C (M = Nb, V, Mo and W) carbide in steels using first-principles calculations. *Acta Mater.* **2012**, *60*, 208–217. DOI:10.1016/j.actamat.2011.09.051
23. Zhang Z, Wang Z, Li Z, Sun X. Microstructure Evolution and Precipitation Behavior in Nb and Nb–Mo Microalloyed Fire-Resistant Steels. *Metals* **2023**, *13*, 112. DOI:10.3390/met13010112
24. Morito S, Nishikawa J, Maki T. Dislocation Density within Lath Martensite in Fe–C and Fe–Ni Alloys. *ISIJ Int.* **2003**, *43*, 1475–1477. DOI:10.2355/isijinternational.43.1475
25. Ning D, Dai CR, Wu JL, Wang YD, Wang YQ, Jing Y, et al. Carbide precipitation and coarsening kinetics in low carbon and low alloy steel during quenching and subsequently tempering. *Mater. Charact.* **2021**, *176*, 111111. DOI:10.1016/j.matchar.2021.111111
26. Hou Z, Babu RP, Hedström P, Odqvist J. Early stages of cementite precipitation during tempering of 1C–1Cr martensitic steel. *J. Mater. Sci*. **2019**, *54*, 9222–9234. DOI:10.1007/s10853-019-03530-8
27. Alaneme KK, Okotete EA. Recrystallization mechanisms and microstructure development in emerging metallic materials: A review. *J. Sci. Adv. Mater. Devices* **2019**, *4*, 19–33. DOI:10.1016/j.jsamd.2018.12.007
28. Sun C, Yang S, Liu G. Evolution of Microstructures of a Low Carbon Bainitic Steel Held at High Service Temperature. *Acta Metall. Sin. (Engl. Lett.)* **2014**, *27*, 436–443. DOI:10.1007/s40195-014-0078-7
29. Janovec J, Svoboda M, Výrostková A, Kroupa A. Time–temperature–precipitation diagrams of carbide evolution in low alloy steels. *Mater. Sci. Eng. A* **2005**, *402*, 288–293. DOI:10.1016/j.msea.2005.04.048
30. Zhang Z, Sun X, Yong Q, Li Z, Wang Z, Wang G. Precipitation behavior of nanometer-sized carbides in Nb–Mo microalloyed high strengh steel and its strengthening mechanism. *Acta Metall. Sin.* **2016**, *52*, 410–418. DOI:10.11900/0412.1961.2015.00482
31. Wang K, Gao G, Gui X, Bai B, Feng C. Comparison of Microstructure and Mechanical Properties of a High-Carbon Bainitic Steel Treated by Long-Time Bainitic Austempering and Short-Time Austempering Plus Tempering Processes. *Steel Res. Int.* **2024**, *95*, 2300501. DOI:10.1002/srin.202300501

32. Muránsky O, Balogh L, Tran M, Hamelin CJ, Park JS, Daymond MR. On the measurement of dislocations and dislocation substructures using EBSD and HRSD techniques. *Acta Mater.* **2019**, *175*, 297–313. DOI:10.1016/j.actamat.2019.05.036
33. Feng C, Wang P, Zhu L, Gui X, Li Z, Gao G. Effect of Microstructure on Corrosion Resistance of Ultralow-Carbon Bainitic Steel. *Steel Res. Int.* **2024**, *95*, 2300720. DOI:10.1002/srin.202300720
34. Kubin LP, Mortensen A. Geometrically necessary dislocations and strain-gradient plasticity: A few critical issues. *Scr. Mater.* **2003**, *48*, 119–125. DOI:10.1016/S1359-6462(02)00335-4
35. Wang Z, Zhang H, Guo C, Liu W, Yang Z, Sun X, et al. Effect of molybdenum addition on the precipitation of carbides in the austenite matrix of titanium micro-alloyed steels. *J. Mater. Sci.* **2016**, *51*, 4996–5007. DOI:10.1007/s10853-016-9804-z
36. Dunlop GL, Honeycombe RKW. The role of dislocations in the coarsening of carbide particles dispersed in ferrite. Philos. Mag. 1975, 32, 61–72. DOI:10.1080/14786437508222805
37. Speich GR, Leslie WC. Tempering of steel. *Metall. Trans.* **1972**, *3*, 1043–1054. DOI:10.1007/BF02642436
38. Macchi J, Teixeira J, Danoix F, Geandier G, Denis S, Bonnet F, et al. Impact of carbon segregation on transition carbides and cementite precipitation during tempering of low carbon steels: Experiments and modeling. *Acta Mater.* **2024**, *272*, 119919. DOI:10.1016/j.actamat.2024.119919
39. Enloe CM, Findley KO, Speer JG. Austenite Grain Growth and Precipitate Evolution in a Carburizing Steel with Combined Niobium and Molybdenum Additions. *Metall. Mater. Trans. A* **2015**, *46*, 5308–5328. DOI:10.1007/s11661-015-3103-1
40. Jiang L, Marceau RKW, Guan B, Dorin T, Wood K, Hodgson PD, et al. The effect of molybdenum on clustering and precipitation behaviour of strip-cast steels containing niobium. *Materialia* **2019**, *8*, 100462. DOI:10.1016/j.mtla.2019.100462
41. Jo HH, Shin C, Moon J, Jang JH, Ha HY, Park SJ, et al. Mechanisms for improving tensile properties at elevated temperature in fire-resistant steel with Mo and Nb. *Mater. Des.* **2020**, *194*, 108882. DOI:10.1016/j.matdes.2020.108882
42. Park H, Jo HH, Kim C, Kim SH, Kim KW, Moon J, et al. Microstructural evolution and strength-toughness behavior of fire-resistant steel under thermo-mechanical controlled processing. *J. Mater. Res. Technol.* **2025**, *37*, 3729–3738. DOI:10.1016/j.jmrt.2025.07.034